

# Towards Generalizable Deepfake Detection via Real Distribution Bias Correction

Ming-Hui Liu, Harry Cheng, Xin Luo, Xin-Shun Xu\* *Senior Member, IEEE*, Mohan S. Kankanhalli *Fellow, IEEE*

**Abstract**—To generalize deepfake detectors to future unseen forgeries, most existing methods attempt to simulate the dynamically evolving forgery types using available source domain data. However, predicting an unbounded set of future manipulations from limited prior examples is infeasible. To overcome this limitation, we propose to exploit the invariance of real data from two complementary perspectives: the fixed population distribution of the entire real class and the inherent Gaussianity of individual real images. Building on these properties, we introduce the Real Distribution Bias Correction (RDBC) framework, which consists of two key components: the Real Population Distribution Estimation module and the Distribution-Sampled Feature Whitening module. The former utilizes the independent and identically distributed (i.i.d.) property of real samples to derive the normal distribution form of their statistics, from which the distribution parameters can be estimated using limited source domain data. Based on the learned population distribution, the latter utilizes the inherent Gaussianity of real data as a discriminative prior and performs a sampling-based whitening operation to amplify the Gaussianity gap between real and fake samples. Through synergistic coupling of the two modules, our model captures the real-world properties of real samples, thereby enhancing its generalizability to unseen target domains. Extensive experiments demonstrate that RDBC achieves state-of-the-art performance in both in-domain and cross-domain deepfake detection.

**Index Terms**—Deepfake Detection, Real Distribution, Distribution Sampling, Generalization.

## I. INTRODUCTION

Advanced image generation models have significantly reduced the barriers to synthesizing realistic images [1], leading to the proliferation of malicious content such as deepfakes [2]. To mitigate this risk, many deepfake detection methods have been proposed to detect obvious artifacts in manipulated images [3]–[8]. These approaches achieve strong performance when trained and tested on datasets from the same domain. However, they are highly prone to overfitting to salient artifacts present in the training set and remain plagued with poor generalization ability, as accuracy drops sharply when encountering unseen forgeries [9].

To alleviate this problem, most previous studies employ data augmentation to expand the source domain forgeries to approximate those in the target domain [10], [11]. These

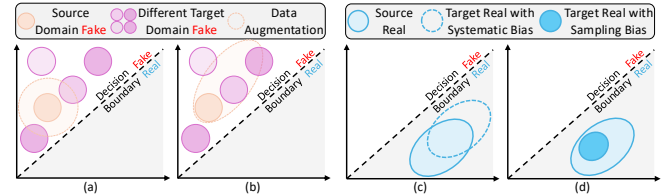


Fig. 1. (a) Direction-agnostic augmentation: the features of fake samples in the source domain are uniformly diffused into the target domain. (b) Direction-aware augmentation: the fake features expand toward specific directions, usually guided by prior knowledge. (c) Systematic Bias: Directional distribution shift induced by hardware constraints (e.g., camera algorithms, sensor noise patterns). (d) Sampling Bias: Distributional shrinkage caused by lack of diversity in demographic attributes (e.g., race, gender, and age).

strategies can be broadly categorized into two types: i) Direction-agnostic augmentation (See Fig. 1(a)), which employs isotropic perturbations, such as affine transformation, to uniformly diffuse the source domain forgeries. ii) Direction-aware augmentation (See Fig. 1(b)), which applies specific forgery cues (e.g., blending artifacts [12]) to extend the source forgeries toward target domains. Although considerable progress has been made [13]–[15], these approaches are built on an implicit assumption: *forgery patterns can be predicted from existing observations*. However, as deepfake techniques evolve rapidly [16], [17], forgeries have become increasingly diverse and unpredictable, rendering this assumption invalid.

Unlike detection models that search for local artifacts, humans distinguish real from fake data by additionally evaluating the consistency between the target data and prior cognitive patterns of real data (*i.e.*, pattern consistency). Here, ‘*real data*’ typically refers to raw sampling signals directly captured by imaging devices. Although imaging technologies continuously evolve (from analog film-based acquisition to digital charge-coupled devices) and exhibit diverse sensor characteristics, their core mechanism remains a high-fidelity mapping of physical-world regularities. Therefore, real data can be abstracted as representations strictly governed by objective physical laws (e.g., optical illumination and reflectance consistency [18], [19], physiological geometry [20], and microscopic hemodynamics [21]). These constraints imply that real data are not arbitrary samples but instead lie on a structured manifold shaped by the statistics of the physical world, as demonstrated by extensive studies [22], [23]. From a statistical perspective, such physically induced regularities result in a consistent population distribution that real data tend to follow.

This highlights a critical insight: compared with the difficult-to-define and continuously evolving distribution of

\* Corresponding author.

Ming-Hui Liu is with the School of Software, Shandong University, Jinan 250101, China, and also with the School of Computing, National University of Singapore, Singapore (e-mail: liuminghui@mail.sdu.edu.cn). Xin-Shun Xu and Xin Luo are with the School of Software, Shandong University, Jinan 250100, China (e-mail: xuxinshun@sdu.edu.cn; luoxin.lxin@gmail.com). Harry Cheng and Mohan S. Kankanhalli are with the School of Computing, National University of Singapore, Singapore (e-mail: xaCheng1996@gmail.com; dcsmk@nus.edu.sg).

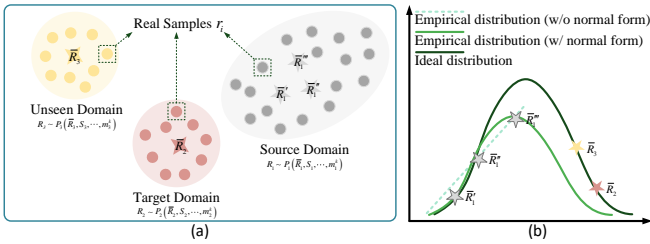


Fig. 2. (a) The distribution of the real data in different domains. (b) The different distribution patterns of a specific statistic (e.g., the ideal distribution, the empirical distribution with the known normal form, and the empirical distribution without a predefined distributional form of the mean  $\bar{R}$ ).

manipulated data (driven by the rapid iterations of generative paradigms such as GANs and Diffusion Models), the distribution manifold of real data, anchored by invariant physical principles, is inherently more deterministic and robust to modeling [22], [24]. This means incorporating prior knowledge of the real data distribution can effectively enhance the ability to identify out-of-distribution (OOD) manipulated fake samples, thereby improving generalization performance.

However, accurately characterizing the global distribution of real data remains highly challenging. In existing deepfake detection datasets, real samples are typically collected from a limited range of device types. Under the combined influence of systematic bias (See Fig. 1(c), e.g. camera-specific ISP algorithms, sensor noise patterns) and sampling bias (See Fig. 1(d), e.g. demographic factors such as race, gender, and age), models tend to overfit the observed data patterns, failing to extract universal distributional characteristics that are independent of specific source samples. As a result, the guidance provided by the real data distribution during feature learning is substantially weakened. Specifically, as illustrated in Fig. 2(a), from a distributional perspective, real data in both the source domain and target domains are essentially non-ideal drawn subsets from the population distribution. Therefore, as shown in Fig. 2(b), the empirical distribution derived from biased source-domain samples (light green dashed line) inevitably deviates from the ideal population distribution (dark green solid line). This distribution shift makes it difficult for the model to adequately cover target-domain samples (colored stars), leading to generalization barriers. To address these challenges, we propose a Real Distribution Bias Correction (RDBC) framework, which approximates the true population distribution of real data as closely as possible (green solid line) to provide more reliable guidance for feature learning.

As shown in Fig. 3, our RDBC framework is built upon two key modules. **i) Real Population Distribution Estimation module.** Since the population distribution of real data is difficult to obtain directly, we instead focus on the distribution of their statistical moments. Theoretically, under ideal independent and identically distributed (i.i.d.) sampling, several statistics of real images follow an asymptotic normal distribution. Based on this distribution form, we estimate the distribution parameters using maximum likelihood estimation. Considering the non-ideal sampling of the source-domain data, we do not attempt to directly estimate the global population

distribution parameters of the real world. Instead, we adopt a predefined distributional form (i.e., the normal distribution) to approximate and extrapolate the envelope of the population distribution in the vicinity of the source-domain distribution, thereby maximizing coverage of target-domain samples. **ii) Distribution-Sampled Feature Whitening module.** After completing the simulation of the population distribution, we incorporate this distributional knowledge into the training process with the Gaussianity of real images as a key insight. Specifically, we construct a whitening matrix by sampling the distribution of the statistics obtained previously. Under the influence of the whitening matrix, the effect of higher-order statistics is strengthened, while the effect of lower-order statistics is weakened. This means the model can better capture the Gaussian nature of images, thereby enhancing the distinguishability between real and fake samples.

In vanilla training settings, limited real data often causes the features to exhibit pronounced clustering patterns (related to background, illumination, or ethnicity) due to overfitting. In contrast, our method dynamically expands the limited source-domain data by injecting distributional knowledge, thereby approximating the ideal scenario in which the model is trained with the complete real-world data. This process encourages the model to shift its focus from superficial correlations to deeper physical-consistency cues, enabling it to learn generalizable criteria for distinguishing between real and fake images. We conduct extensive experiments on several widely used deepfake detection datasets, and the results demonstrate that our approach outperforms several existing state-of-the-art (SoTA) methods. Our main contributions are threefold:

- To the best of our knowledge, we are the first to examine the generalization problem in deepfake detection from a distribution perspective and leverage the real image population distribution to enhance performance of detectors.
- We propose the Real Distribution Bias Correction framework, which first demonstrates that the statistics of real images follow the normal distribution. Then it enhances the distinguishability between real and fake samples via the Gaussianity of the image samples.
- Extensive experiments demonstrate the effectiveness of our method. The proposed method can be easily integrated with various backbone networks.

## II. RELATED WORK

### A. Deepfake Generation and Detection

**Generation.** Deepfake generation has rapidly evolved with advances in portrait and image synthesis. Early methods rely on autoencoders [25], which train two separate encoder-decoder models (one per identity) for facial reconstruction and then swap decoders to transfer identities [26], [27]. Although effective, these models are limited to one-to-one swaps. Subsequently, Generative Adversarial Networks (GANs) are employed, significantly enhancing the realism and flexibility of deepfake generation [28]–[35]. Recently, diffusion models have introduced a new paradigm for high-fidelity synthesis [16], [36]. For instance, DiffSwap formulates face swapping as a conditional image inpainting task [37]. The

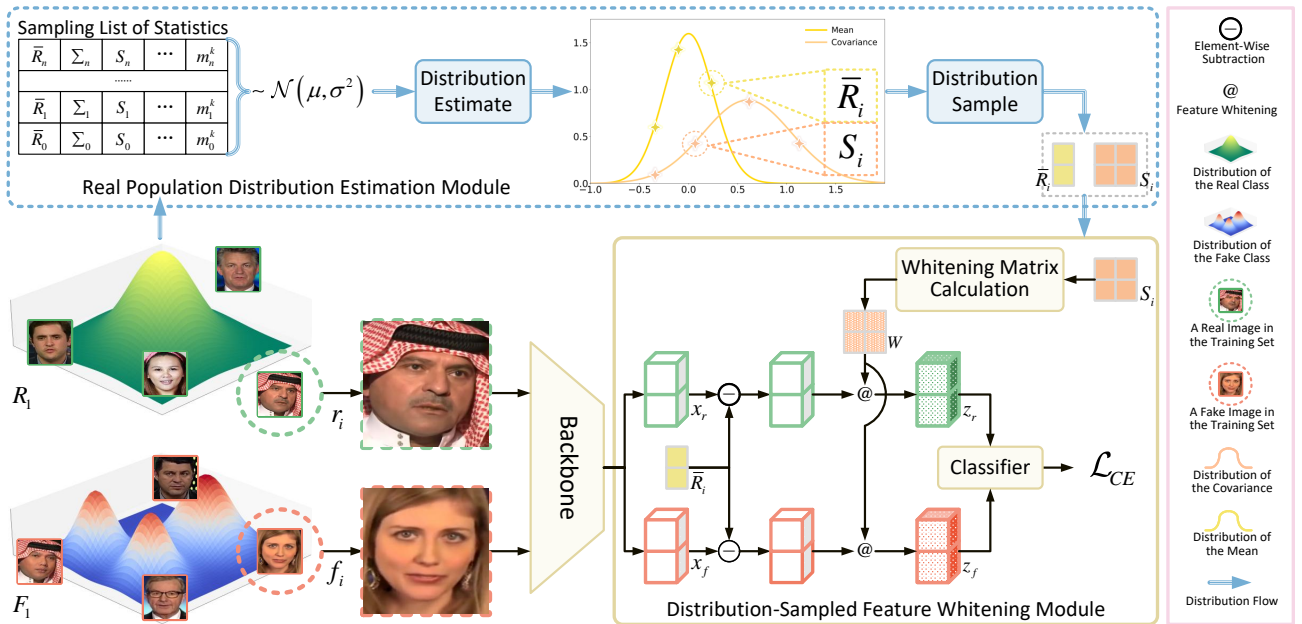


Fig. 3. Our RDDB framework consists of two components: i) Real Population Distribution Estimation Module estimates the distribution form and calculates its parameters based on MLE. ii) Distribution-Sampled Feature Whitening Module takes the Gaussianity as a discriminative cue and enhances the Gaussian discrepancy between real and fake images through a distribution-sampled whitening operation.

development of generative techniques has led to increasingly diverse types of deepfake forgeries, making it inherently infeasible to predict future forgeries. This motivates our work to instead focus on real images, which follow a more stable and consistent distribution.

**Detection.** Deepfake detection is commonly formulated as a binary classification problem [5], [38]–[40]. Early studies primarily focus on identifying dataset-specific forgery artifacts [41]–[43], yielding strong intra-dataset performance but poor generalization across different domains. To overcome this limitation, a growing body of work has sought to capture more generalizable artifact patterns following the data augmentation paradigm [3], [5], [9], [9], [44]–[46]. Some methods attempt to uniformly broaden the data distribution within the source domain to enhance the model’s exposure to diverse forgery types. For example, incorporating attention maps [13], [47] or external tools such as large language models (LLMs) [48] into forgery samples. In contrast, other methods focus on augmentations derived from specific or predefined forgery traces, such as highlighting blending boundaries [11], [12] or identifying multi-modal inconsistencies [14], [49]. In general, these approaches aim to improve generalizability by predicting the distribution of unseen forgeries. Nevertheless, the instability of forgery distributions presents a fundamental limitation. Therefore, we turn our attention to the real data population distribution as an alternative means to enhance generalization.

### B. Real-world Images Properties

In this paper, we consider the invariance exhibited both in the population distribution and structure of real-world images as the primary motivation to address the generalization issue. From the population distribution view, the real-world images

have the i.i.d. nature, which has formed the theoretical foundation of numerous computer vision methods [23], [50]–[52]. For instance, Zhong *et al.* [53] demonstrate that real images encode consistent cues from the camera imaging pipeline, where predicting EXIF metadata reflecting physical imaging parameters enables models to learn camera-intrinsic representations, further indicating that authentic photographs follow stable physical regularities that synthetic images often fail to reproduce. Ballé *et al.* [54] models images as i.i.d. sources to optimize image compression. Regarding the internal structure of real images, studies have shown that although natural images are not strictly Gaussian, they often exhibit approximately Gaussian statistical behavior at the aggregate level [50], [55]. Specifically, when numerous independent pixel-level factors are combined, the resulting distribution tends toward Gaussianity. Based on this, image patches, transform coefficients, or noise can be considered to have some Gaussian properties (or mixtures of Gaussians) [23], [55], [56]. For instance, camera sensor noise is modeled as additive white Gaussian noise [57].

## III. METHODOLOGIES

### A. Overview

Ideally, since real data are captured by optical cameras and governed by objective physical laws, they are expected to be i.i.d. samples drawn from a consistent *population distribution*. However, existing datasets are often constrained by specific data collection protocols, introducing unavoidable systematic biases (*e.g.*, sensor configurations) and sampling biases (*e.g.*, limited demographic diversity). As a result, real data in different datasets are essentially biased subsets rather than ideal i.i.d. samples. These biases cause their *empirical distributions* to deviate from one another, reflecting significant domain gaps and generalization bottlenecks.

To overcome this challenge, in this paper, we introduce the Real-Distribution Bias Correction (RDBC) framework. Our approach comprises two modules: **i) Real Population Distribution Estimation** and **ii) Distribution-Sampled Feature Whitening**. As shown in Fig. 3, the first module exploits the i.i.d. property of ideal real data and derives that certain statistics (*e.g.*, the mean and covariance) follow an asymptotic normal distribution. This distributional form is then used as a prior to approximate the population distribution in the vicinity of the biased source-domain data via maximum likelihood estimation (MLE). Based on the estimated population distribution, the second module leverages the Gaussianity of real data as a discriminative cue and enhances the Gaussian discrepancy between real and fake data through a distribution-sampled whitening operation. By focusing on the statistical properties of real data, our framework corrects the bias in the observed distribution, effectively incorporates distributional knowledge into training, and improves generalization ability. The following subsections describe the two modules in detail.

### B. Real Population Distribution Estimation

**Revisiting Deepfake Generalization.** As illustrated in Fig. 2, from a statistical perspective, all real images  $\{r_i\}_{i=1}^N$  in a single deepfake detection dataset can be viewed as a set of random samples drawn from the entire set of real data  $\mathbb{R}$  from the real-world. Under ideal sampling conditions, each image  $r_i$  can be viewed as an i.i.d random variable:

$$r_i \stackrel{\text{i.i.d.}}{\sim} P_{\mathbb{R}}(r), \quad i = 1, \dots, N, \quad (1)$$

where  $P_{\mathbb{R}}$  is the fixed population distribution of  $\mathbb{R}$ . For real data from different domains (*e.g.*, all of the real data  $R_1$  in the training set and  $R_2$  in the testing set), although they originate from the same population  $\mathbb{R}$ , they may exhibit different distributions due to systematic bias and sampling bias. This means the uniquely determined statistical characteristics computed from the training set (*e.g.*, sample mean  $\bar{R}_1$  and covariance  $S_1$ ) will differ from those derived from the testing set (*e.g.*, sample mean  $\bar{R}_2$  and covariance  $S_2$ ):

$$\bar{R}_1 \neq \bar{R}_2, \quad S_1 \neq S_2, \quad (2)$$

where the mean  $\bar{R}$  and the covariance  $S$  are defined as:

$$\bar{R} = \frac{1}{N} \sum_{i=1}^N r_i, \quad (3a)$$

$$S = \frac{1}{N-1} \sum_{i=1}^N (r_i - \bar{R})(r_i - \bar{R})^\top. \quad (3b)$$

These distinct statistical characteristics will constitute different sampling distributions  $P_1$  and  $P_2$ , and lead to generalization issues in the deepfake detection task:

$$P_1(\bar{R}_1, S_1, \dots, m_1^k) \neq P_2(\bar{R}_2, S_2, \dots, m_2^k), \quad (4)$$

where  $m_1^k$  and  $m_2^k$  are the  $k$ -th order statistics corresponding to the sampling distributions  $P_1$  and  $P_2$ , respectively.

However, it is important to note that despite exhibiting different statistics, the real images of different domains originate from the same population  $\mathbb{R}$ . Once the population distribution

$P_{\mathbb{R}}$  is known, the model can confirm whether an arbitrary sample conforms to the distribution, thereby facilitating the detection of out-of-distribution fake samples. Therefore, it is reasonable to disregard  $P_1$  and  $P_2$ , and instead analyze the generalization issue from the perspective of  $P_{\mathbb{R}}$ :

**Inference 1:** Once the population distribution  $P_{\mathbb{R}}$  of real data is learned, any real test sample drawn from this distribution is distributionally familiar to the model.

With knowledge of population distribution  $P_{\mathbb{R}}$ , the complex cross-domain task can be effectively transformed into a simpler in-domain problem. To this end, we first investigate how to model the population distribution of the real class and then estimate its parameters using the limited training data.

**Form of the Real Population Distribution.** Ideally, the real population distribution  $P_{\mathbb{R}}$  could be estimated from the complete set of real-world images. However, such estimation is infeasible under limited training data. Therefore, we introduce and further generalize the Central Limit Theorem (CLT) to infer the population distribution of real data:

**Theorem 1 (Generalized CLT):** Given a sufficient number of i.i.d. random variables, the distribution of specific statistics asymptotically converges to a normal distribution.

Within the context of deepfake detection task, the generalized CLT [58] guarantees that, regardless of the original distribution of the total real data  $\mathbb{R}$ , the distributions of the mean  $\bar{R}$  and the covariance  $S$  of a large batch of i.i.d. real images  $\{r_i\}_{i=1}^N$  always converge to the normal distributions  $\mathcal{N}_{\bar{R}}$  and  $\mathcal{N}_S$  with their own parameters:

$$\sqrt{N}(\bar{R} - \mu) \xrightarrow{d} \mathcal{N}_{\bar{R}}(0, \sigma^2), \quad (5a)$$

$$\sqrt{N} \text{vec}(S - \Sigma) \xrightarrow{d} \mathcal{N}_S(0, V), \quad (5b)$$

where  $N$  is the sample size of real images.  $\mu$  and  $\sigma$  are the mean and standard deviation of the distribution  $\mathcal{N}_{\bar{R}}$ , respectively.  $\Sigma$  and  $V$  are the covariance matrix of the distribution  $\mathcal{N}_S$  and the asymptotic covariance matrix of  $S$ , respectively.  $\text{vec}(\cdot)$  denotes the matrix vectorization operation.

By invoking the ideal sampling condition and the generalized CLT, we observe that although the mean values  $\bar{R}_1$  and  $\bar{R}_2$  (or the covariance values  $S_1$  and  $S_2$ ) vary across different datasets, they can still be regarded as sampled points drawn from an underlying normal distribution (*e.g.*,  $\mathcal{N}_{\bar{R}}$  and  $\mathcal{N}_S$ ):

$$\bar{R}_1, \bar{R}_2 \sim \mathcal{N}_{\bar{R}}(\mu_{\bar{R}}, \sigma_{\bar{R}}^2), \quad (6a)$$

$$S_1, S_2 \sim \mathcal{N}_S(\mu_S, \sigma_S^2), \quad (6b)$$

where the parameters  $(\mu_{\bar{R}}, \sigma_{\bar{R}}^2)$  and  $(\mu_S, \sigma_S^2)$  can be calculated by the ideal-sampled real data. Since then, we replace the intractable distribution  $P_{\mathbb{R}}$  of real samples themselves with the estimable distribution of the statistics (*e.g.*,  $\mathcal{N}_{\bar{R}}$  and  $\mathcal{N}_S$ ).

**Parameters of the Real Population Distribution.** Although the normal distribution is derived under ideal sampling assumptions, we can still estimate its parameters using biased training data. While this does not recover the true distributions in the real world, it can serve as prior knowledge to regularize and extrapolate the envelope of the empirical distribution.

Specifically, for the normal distribution  $\mathcal{N}(\mu, \sigma^2)$  considered in this work, we can employ maximum likelihood esti-

mation (MLE) to determine the distribution parameters, and its log-likelihood function is given by:

$$\ell(\mu, \sigma^2) = -\frac{N}{2} \ln(2\pi) - \frac{N}{2} \ln(\sigma^2) - \frac{1}{2\sigma^2} \sum_{i=1}^N (x_i - \mu)^2. \quad (7)$$

In practice,  $\{x_i\}_{i=1}^N$  is a set of statistical values (e.g., the mean values  $\{\bar{R}_i\}_{i=1}^N$  or covariance values  $\{S_i\}_{i=1}^N$ ) calculated using a batch of real image vectors repeatedly sampled from the training set. From Equation (7), we can obtain the related maximum likelihood estimators  $\hat{\mu}$  and  $\hat{\sigma}^2$  by taking the partial derivatives with respect to  $\mu$  and  $\sigma^2$ , and then setting them to zero for solving the extrema:

$$\frac{\partial \ell}{\partial \mu} = \frac{1}{\sigma^2} \sum_{i=1}^N (x_i - \mu) = 0, \quad (8a)$$

$$\frac{\partial \ell}{\partial \sigma^2} = -\frac{n}{2\sigma^2} + \frac{n}{2(\sigma^2)^2} \sum_{i=1}^N (x_i - \mu)^2 = 0. \quad (8b)$$

By solving Equation (8), the closed-form maximum likelihood estimators for the normal distribution  $\mathcal{N}$  are:

$$\hat{\mu} = \frac{1}{N} \sum_{i=1}^N x_i, \quad \hat{\sigma}^2 = \frac{1}{N} \sum_{i=1}^N (x_i - \hat{\mu})^2. \quad (9)$$

To determine what distributions the statistics (e.g., the mean  $\bar{R}$  and covariance  $S$ ) follow, we substitute  $x_i$  with specific mean values  $\{\bar{R}_i\}_{i=1}^N$  and covariance values  $\{S_i\}_{i=1}^N$  into Equation (9) to solve for parameter values as follows:

$$\hat{\mu}_{\bar{R}} = \frac{1}{N} \sum_{i=1}^N \bar{R}_i, \quad \hat{\sigma}_{\bar{R}}^2 = \frac{1}{N} \sum_{i=1}^N (\bar{R}_i - \hat{\mu}_{\bar{R}})^2, \quad (10a)$$

$$\hat{\mu}_S = \frac{1}{N} \sum_{i=1}^N S_i, \quad \hat{\sigma}_S^2 = \frac{1}{N} \sum_{i=1}^N (S_i - \hat{\mu}_S)^2, \quad (10b)$$

where  $(\hat{\mu}_{\bar{R}}, \hat{\sigma}_{\bar{R}}^2)$  and  $(\hat{\mu}_S, \hat{\sigma}_S^2)$  denote the maximum likelihood estimators of distributions  $\mathcal{N}_{\bar{R}}$  and  $\mathcal{N}_S$ , respectively. For brevity, we represent the distributions of  $\bar{R}$  and  $S$  as follows:

$$\bar{R}_i \sim \mathcal{N}_{\bar{R}}(\hat{\mu}_{\bar{R}}, \hat{\sigma}_{\bar{R}}^2), \quad S_i \sim \mathcal{N}_S(\hat{\mu}_S, \hat{\sigma}_S^2). \quad (11)$$

It is worth noting that  $\mathcal{N}_{\bar{R}}$  or  $\mathcal{N}_S$  is a population distribution encompassing the full variability of real data, and each sample drawn from it corresponds to a statistical representation of real data from a specific target domain.

### C. Distribution-Sampled Feature Whitening

After obtaining the exact population distribution for several statistics of the entire set of real data  $\mathbb{R}$ , we aim to incorporate this distributional knowledge into the training process. Specifically, we design a distribution-sampled whitening operation that simultaneously enlarges the Gaussianity difference between real and fake data while exposing all possible target domain distributions during training.

**Gaussianity gap between real and fake data.** As shown in Fig. 4, constrained by physical image formation and sensor noise mechanisms, a real image  $r_i \in \mathbb{R}$  exhibits near-Gaussian and weakly correlated patterns in the content-independent domain. As a result, its distribution is fully determined by

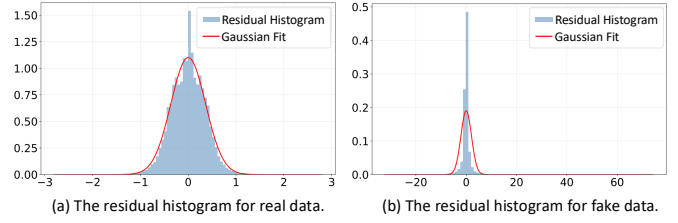


Fig. 4. Comparisons between the residual histograms. Compared with real images, the fake ones exhibit pronounced leptokurtosis and skewness, demonstrating non-Gaussian characteristics.

the mean  $\mu$  and variance  $\sigma^2$ , while all higher-order cumulants vanish. In contrast, the fake image  $f_i \in \mathbb{F}$  lacks authentic device noise, leading to significant deviations from Gaussianity, and its distribution characteristics are governed by higher-order statistical moments [59], [60].

**Enhancing Gaussianity through Whitening.** To leverage this disparity in Gaussian characteristics for distinguishing between real and fake images, we introduce a whitening transformation, which eliminates the influence of low-order statistics (i.e.,  $\mu$  and  $\sigma^2$ ) via a whitening matrix  $W_{c \times c}$ :

$$W = \frac{1}{\sqrt{S}}, \quad (12)$$

where  $S_{c \times c}$  is the covariance matrix calculated by real data.  $c$  represents the feature dimension. Then, the whitening matrix  $W$  is applied to both the original real and features  $\mathbf{x} \in \mathbb{R} \cup \mathbb{F}$ . For real data, it highlights the Gaussian components. For fake data, it amplifies the higher-order non-Gaussian components:

$$\mathbf{z} = W(\mathbf{x} - \mu), \quad (13)$$

where  $\mu_{1 \times c}$  is the mean vector of the original real features.  $\mathbf{z}_{1 \times c}$  is the whitened feature, which is guaranteed to have zero mean and an identity covariance matrix:

$$\mathbb{E}[\mathbf{z}] = 0, \quad \text{Cov}(\mathbf{z}) = I. \quad (14)$$

After the feature whitening operation, the whitened feature  $\mathbf{z}$  becomes independent of low-order statistics. If the original feature  $\mathbf{x}$  follows a Gaussian distribution (corresponding to the real class), its whitened feature will preserve Gaussianity and further conform to a standard normal distribution  $\mathcal{N}(0, 1)$ . If the original feature is non-Gaussian (corresponding to the fake class), the whitening process removes the influence of low-order statistics, thereby amplifying the remaining higher-order non-Gaussian components.

**Random Whitening via Distribution Sampling.** In traditional implementations, the covariance matrix  $S$  used for whitening is a deterministic quantity computed from all real samples  $\{r_i\}_{i=1}^N$  in the training set as:

$$S = \frac{1}{N} (R - \bar{R})(R - \bar{R})^\top, \quad (15)$$

where  $R_{N \times c}$  denotes the feature matrix stacked by  $N$  real vectors, and  $\bar{R}_{1 \times c}$  denotes the mean of these  $N$  real vectors. However, due to sampling discrepancies between the source and target domains, directly using the covariance matrix  $S$  computed by the training data may cause overfitting to the

TABLE I

PERFORMANCE COMPARISON (%). ALL MODELS ARE TRAINED ON THE FF++ DATASET. THE BEST PERFORMANCE IS MARKED IN BOLD. †: WE RE-IMPLEMENT THE DETECTOR. \*: THE METHOD FOCUSES ON AUGMENTING REAL IMAGES. -: THE RELEVANT RESULTS ARE NOT REPORTED IN THE ORIGINAL PAPER.

Method	Venue	Testing Dataset					
		FF++	Celeb-DF	DFDC	DFDCp	UADFV	AVG
†EfficientNet [61]	ICML'19	96.67	64.59	65.43	80.27	63.19	68.37
†Face X-ray [62]	CVPR'20	95.72	74.76	61.57	71.15	64.34	67.95
†CORE [63]	CVPRW'22	96.61	79.45	62.60	75.74	65.41	70.80
†RECCE [64]	CVPR'22	96.95	69.71	62.82	74.19	78.61	71.33
†SBI* [12]	CVPR'22	85.16	93.18	72.42	86.15	97.28	87.76
†CADDM [65]	CVPR'23	97.16	91.63	63.77	80.22	97.32	83.24
†UCF [66]	ICCV'23	97.16	81.90	66.21	80.94	97.15	81.55
FoCUS [67]	TIFS'24	99.15	76.13	68.42	76.62	-	-
Qiao et al. [68]	TPAMI'24	99.00	70.00	-	-	78.00	-
GRU [69]	CVPR'24	98.40	89.00	-	-	-	-
ProDet [15]	NeurIPS'24	95.91	84.48	72.40	81.16	-	-
†FreqBlender* [70]	NeurIPS'24	93.29	92.65	73.15	84.56	94.79	86.29
†Effort [71]	ICML'25	98.85	93.68	74.49	86.22	98.07	88.62
†VLFFD [48]	CVPR'25	98.64	89.80	71.80	84.74	96.71	85.76
†FIA-USA [72]	NeurIPS'25	98.71	93.52	79.24	85.68	97.89	89.08
<b>RDBC</b>	-	<b>99.41</b>	<b>96.03</b>	<b>82.68</b>	<b>89.32</b>	<b>99.23</b>	<b>91.82</b>

source domain. Therefore, in practical whitening operation, the fixed source-domain covariance matrix  $S$  in Equation (15) and mean vector  $\mu$  in Equation (13) are substituted by a random sampling  $S'$  and  $\mu'$ :

$$S' \sim \mathcal{N}_S(\hat{\mu}_S, \hat{\sigma}_S^2), \quad (16a)$$

$$\mu' \sim \mathcal{N}_{\bar{R}}(\hat{\mu}_{\bar{R}}, \hat{\sigma}_{\bar{R}}^2), \quad (16b)$$

where  $\mathcal{N}_S(\hat{\mu}_S, \hat{\sigma}_S^2)$  and  $\mathcal{N}_{\bar{R}}(\hat{\mu}_{\bar{R}}, \hat{\sigma}_{\bar{R}}^2)$  denote the distributions defined in Equation (11), which characterize all the possible covariance matrices in the real-world. Finally, the whitening operation in Equation (13) is ultimately transformed into a distribution-sampled formulation as:

$$\mathbf{z} = \frac{(\mathbf{x} - \mu')}{\sqrt{S'}}. \quad (17)$$

By sampling different  $S'$  and  $\mu'$ , the model is no longer constrained by a fixed source pattern. Through the injection of diverse real-world distribution knowledge, the broader representations that may be encountered during testing can be effectively seen in advance during training.

#### D. Training and Evaluation Protocols

**Warm-up.** Before each epoch, we randomly sample a sufficient number of real images from the training set  $\mathcal{D}$ , and use their features to compute the population distribution  $\mathcal{N}_{\bar{R}}$  and  $\mathcal{N}_S$  following Equation (9) and Equation (11). Subsequently, the estimated distributions are stored to support the whitening operation during the training phase.

**Training.** For each mini-batch, the whitening operation is applied to both the real and fake features following Equation (17). Meanwhile, the relative statistics  $\mu'$  and  $S'$  are sampled from the population distribution  $\mathcal{N}_{\bar{R}}$  and  $\mathcal{N}_S$  computed in the warm-up phrase. Finally, the whitened features  $\mathbf{z}$  are used

for deepfake detection, and the classifier  $f_{\theta}(\cdot)$  is optimized via the cross-entropy loss:

$$\mathcal{L}_{\text{CE}} = -\frac{1}{|\mathcal{D}|} \sum_{\mathbf{z} \in \mathcal{D}} y \log f_{\theta}(\mathbf{z}), \quad (18)$$

where  $y$  denotes the ground-truth label of each image, and  $|\cdot|$  represents the number of samples in the set.

**Inference.** In the testing stage, we load the stored checkpoint which contains both the model parameters and the estimated real population distributions. Before classification, we perform the whitening operation on both the real and fake features.

## IV. EXPERIMENTS

### A. Datasets and Implementation Details

Following the common setting [4], [11], [73], we train our model on the FaceForensics++ (FF++) dataset (c23 version) [74]. It consists of 1,000 real videos and 5,000 manipulated videos generated using five forgery methods, *i.e.*, Deepfakes (DF), FaceSwap (FS), Face2Face (F2F), FaceShifter (Fsh), and NeuralTextures (NT), resulting in a total of 6,000 videos. Furthermore, four widely used deepfake datasets, *i.e.*, Celeb-DF [75], DFDC [76], DFDCp, and UADFV [77], represent the target domain to evaluate the generalizability.

We extract faces from the images and resize them to  $224 \times 224$  pixels for both the training and testing sets. Our experiments are conducted on a single H100 GPU with a batch size of 32, and the EfficientNet [61] is used as the backbone. In addition, to demonstrate the robustness of the proposed approach, we switch the backbone to other networks, *e.g.*, Xception [74] and ViT [78] in Section IV-C.

### B. Performance Comparison

**Main Results.** We present the comparison results between our proposed method and SoTA models in Table I. All of them are trained on FF++ and evaluated on five testing datasets,

TABLE II

AUC (%) COMPARISON OF APPLYING RDBC TO DIFFERENT BACKBONES. ViT-L AND ViT-B REPRESENT DIFFERENT SCALES OF THE ViT.

Backbone	FF++	Celeb-DF	DFDC	DFDCp	UADFV
Xception	96.37	56.75	64.19	72.17	62.05
Xception (SBI)	77.50	90.11	70.16	73.19	94.12
Xception (RDBC)	<b>98.25</b>	<b>92.44</b>	<b>73.50</b>	<b>76.29</b>	<b>95.13</b>
ViT-L (O)	97.65	77.27	64.54	78.05	76.13
ViT-L (SBI)	70.32	88.26	71.98	84.60	93.71
ViT-L (RDBC)	<b>99.20</b>	<b>91.00</b>	<b>75.97</b>	<b>86.08</b>	<b>94.92</b>
ViT-B (O)	98.38	89.63	68.00	80.04	80.17
ViT-B (SBI)	89.64	93.54	73.63	84.87	92.04
ViT-B (RDBC)	<b>99.21</b>	<b>95.26</b>	<b>76.59</b>	<b>86.47</b>	<b>95.05</b>

TABLE III

ROBUSTNESS EVALUATION (AUC %) AGAINST COMMON IMAGE CORRUPTIONS ON THE CELEB-DF DATASET. THE BEST RESULTS ARE MARKED IN **BOLD**.

Method	Clean	JPEG Compression		Gaussian Blur	Gaussian Noise
		Q = 70	Q = 50	$\sigma = 3$	$\sigma^2 = 0.01$
EfficientNet	64.59	58.24	52.18	54.33	51.87
CADDM	91.63	82.15	73.40	76.82	70.55
SBI	93.18	84.62	75.31	78.45	76.20
Effort	93.68	87.35	80.12	82.64	79.88
<b>RDBC</b>	<b>96.03</b>	<b>93.41</b>	<b>88.75</b>	<b>90.22</b>	<b>87.64</b>

covering both the source and target domains. We employ the Area Under the Curve (AUC) metric to evaluate performance on each individual data set and also report the average AUC across the target domain testing datasets.

**Comparison with SoTA detectors.** Table I shows that our method achieves significant improvements in both detection accuracy in the source domain and generalization performance in the target domain. For instance, on the FF++ dataset, our approach reaches near-saturated performance. On the DFDC dataset, it achieves an AUC score of 82.68%, outperforming all of the baselines. This demonstrates that our method effectively tackles the generalization issues.

**Comparison with real image augmentation approaches.** Some methods focus on enhancing the generalization ability by performing data augmentation on real samples from the source domain (marked with ‘\*’ in Table I). We also conduct comparisons with these methods, and the results show that their performance still falls short of our RDBC. One critical reason is that these approaches are designed to add prior knowledge into real images to simulate forgery traces, *i.e.*, they are still predicting ‘forgery patterns.’ In contrast, our method focuses on the distribution of statistics derived from real images, offering better generalization.

It is worth noting that these methods exhibit poor performance in the source domain. For instance, SBI achieves only 85% AUC on the FF++ dataset. This is because their enhancement strategies for real images do not effectively improve the discriminability between real and fake data, especially in the source domain. In contrast, our approach amplify the Gaussianity gap between real and fake images, thereby maintaining the source domain performance.

TABLE IV

AUC (%) COMPARISON OF DIFFERENT MODULES. RDE: REAL DISTRIBUTION ESTIMATION MODULE. FW: FEATURE WHITENING MODULE.

Backbone	RDE	FW	Testing Set			
			FF++	Celeb-DF	DFDC	DFDCp
✓			96.67	64.59	65.43	80.27
✓		✓	99.00	84.13	76.28	84.52
✓	✓	✓	99.41	96.03	82.68	89.32

TABLE V

ACC (%) COMPARISON OF REAL IMAGES ACROSS DIFFERENT MODELS ON THE SOURCE AND TARGET DOMAINS.

Method	FF++	Celeb-DF	DFDC	DFDCp	UADFV
Xception	85.14	27.61	61.76	44.68	55.10
EfficientNet	85.28	31.43	52.71	60.17	61.22
CADDM	87.93	26.29	60.62	70.49	81.63
SBI	80.50	28.11	61.63	67.59	85.71
<b>RDBC</b>	<b>90.68</b>	<b>39.62</b>	<b>62.82</b>	<b>80.89</b>	<b>91.84</b>

### C. Ablation Studies

**Comparison with Different Backbones.** Our method estimates the population distribution of real images by computing the distribution of their statistics. It requires no model modification and is thus model-agnostic. To evaluate this, we incorporate RDBC into different backbone networks, *i.e.*, Xception [74], ViT-L-32 [78], and ViT-B-16. For comparison, we also include SBI, a method that enhances generalization by augmenting real images, as a baseline. As shown in Table II, our method consistently improves the performance across all backbones. For instance, based on Xception, RDBC increases the AUC score on Celeb-DF by 36%. When based on ViT-L, it yields an average improvement of 10%. Notably, while SBI offers some improvement in generalization, it often leads to a decline in intra-domain performance across these backbones. In contrast, RDBC achieves improved generalization and robust intra-domain performance.

**Robustness against Image Degradations.** In real-world scenarios, images and videos inevitably undergo various post-processing operations during transmission, such as compression, blurring, and noise injection. These operations may corrupt the artifacts that many deepfake detectors rely on, leading to severe distribution shifts and performance degradation. To evaluate the robustness of our method under such realistic corruptions, we performed experiments on the Celeb-DF dataset with three common degradations: JPEG compression (Quality = 70 and 50), Gaussian blur ( $\sigma = 3$ ) and Gaussian noise ( $\sigma^2 = 0.01$ ). The robustness evaluation results are presented in Table III. As observed, baseline methods that heavily rely on mining local forgery artifacts or blending boundaries suffer catastrophic performance drops when facing severe degradations. For instance, under JPEG compression with  $Q = 50$ , the AUC of SBI drops by more than 17%, as the artifacts introduced by extreme compression act as a low-pass filter, obfuscating the subtle forgery traces. In contrast, our RDBC exhibits remarkable resilience across all types of corruptions, maintaining an AUC of 88.75% even under severe JPEG

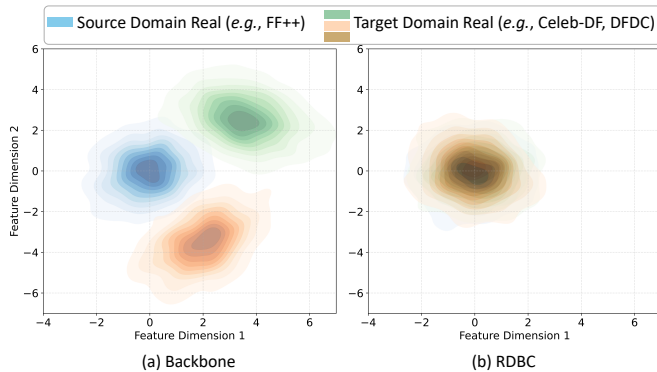


Fig. 5. KDE visualization of real image features from different domains. (a) **Backbone**: The target features deviate severely from the source. (b) **RDBC**: Scattered features are aligned into a unified distribution using our method.

compression ( $Q = 50$ ) and outperforming the second-best method by a significant margin. This exceptional robustness essentially stems from our core motivation: instead of tracking fragile microscopic artifacts, RDBC captures the macroscopic, high-order statistical properties (*i.e.*, Gaussianity) of real images. Since the global statistical distribution of real data is inherently more stable and less sensitive to local pixel-level perturbations, our distribution-sampled feature whitening module consistently maintains the distinctiveness between real and fake features, regardless of the applied physical degradations.

**Module Analysis.** We report on the ablation study of the modules in RDBC in Table IV. Specifically, our RDBC employs a randomly sampled whitening matrix on top of the backbone during training. To evaluate its effectiveness, we compare it with a variant where the whitening matrix is computed using fixed sampling, that is, it is directly derived from real features (as shown in Equation (15) rather than sampled from the estimated distribution. As shown in the table, using a fixed whitening matrix (*i.e.*, *backbone + FW*) provides a certain performance gain over the backbone. This improvement can be attributed to the whitening matrix’s ability to eliminate low-order statistics, thereby enhancing the discriminability between real and fake features. When random sampling is introduced (*i.e.*, *backbone + RDE + FW*), the model achieves a further performance boost. For example, it yields a 6% improvement in AUC on DFDC. This suggests that random sampling enriches the prior of the whitening matrix, enhancing the model’s perception of the real class. In summary, incorporating all of our proposed strategies can achieve the best performance.

**Performance on Real Images.** We report the performance of the models on real images only in Table V. Since this evaluation involves a single class, we use ACC as the primary metric. As shown in the table, the baselines perform poorly on real images. For instance, Xception achieves only 27% accuracy on Celeb-DF. This can be attributed to the fact that existing methods focus on modeling fake patterns while neglecting accurate representations of real data. In contrast, our method is designed to model the distribution of real images, leading to significantly improved accuracy on real samples. For instance, on DFDCp, our approach improves real image accuracy by at least 10% compared to all baselines.

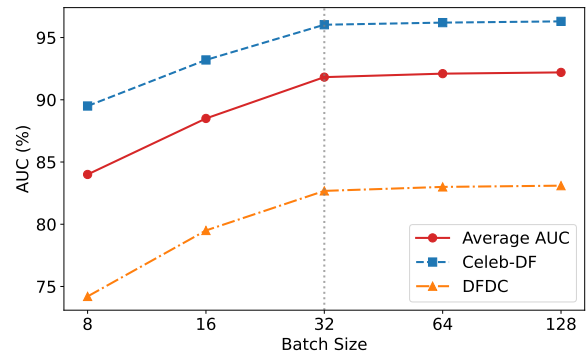


Fig. 6. Comparison on the batch size ( $N$ ) used for real distribution estimation during training. The performance rapidly converges at  $N = 32$ , demonstrating that our method is highly effective even under limited sample sizes.

To illustrate how our method overcomes the domain shifts and achieves generalization, we visualize the 2D Kernel Density Estimation (KDE) contour plots of the extracted real features in Fig. 5. Specifically, real images from varying target domains inevitably suffer from *systematic bias* and *sampling bias*. As shown in Fig. 5(a), due to these biases, the real feature distributions of the baseline model extracted from varying target domains deviate severely from the source domain, scattering into disjoint, non-overlapping clusters. In contrast, Fig. 5(b) demonstrates that after applying our RDBC framework, these previously scattered clusters are seamlessly unified. This indicates that our method filters out both systematic and sampling biases, abstracting a dataset-agnostic, invariant population distribution of real-world data.

**Impact of Sample Size.** Theoretically, the application of the Generalized CLT relies on the asymptotic behavior of statistics as the sample size approaches infinity ( $N \rightarrow \infty$ ). However, in practical implementations, the observable sample size is strictly constrained by the mini-batch size. To investigate whether our RDBC remains robust under limited sample sizes, we conduct an experiment by varying the batch size  $N \in \{8, 16, 32, 64, 128\}$  used to calculate the statistical moments (mean and covariance) of real images. As illustrated in Fig. 6, our model exhibits a clear convergence trend with respect to  $N$ . When the sample size is small (*e.g.*,  $N = 8$ ), the estimated covariance matrix is prone to high variance, which slightly hampers the cross-domain performance. However, as  $N$  increases to our default setting of 32, the average cross-domain AUC score rapidly plateaus and stabilizes. Further expanding the sample size to 64 or 128 yields marginal performance improvements while incurring heavier computational overhead during the warm-up and training phases. This validates that an exact infinite sample size is not a strict prerequisite. A moderately sized batch (*i.e.*,  $N = 32$ ) is sufficient to obtain an accurate and stable approximation of the true population distribution of real data.

#### D. Visualization

**Heatmaps.** Fig. 7 presents the heatmaps generated by the backbone method and our method. The heatmaps from each

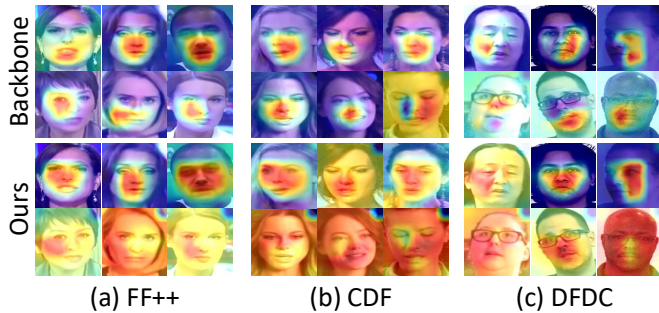


Fig. 7. The heatmaps on different datasets. For each method, the first row shows the heatmaps of real images, while the second row shows those of fake images. The intensity of the red color indicates the level of attention.

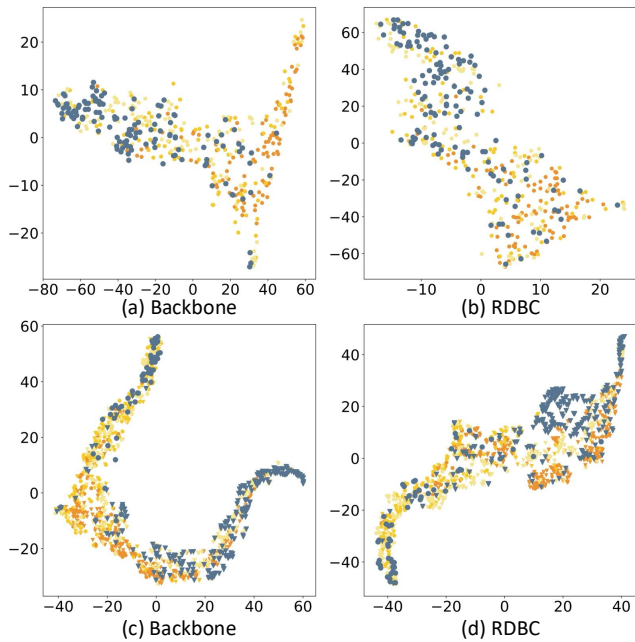


Fig. 8. t-SNE comparison of image features from the source and target domains. (a) and (b): comparison of real images. (c) and (d): comparison of both real and fake images.

approach are organized into two rows: the first row corresponds to real samples, and the second to fake samples. From the figure, we observe that: i) When analyzing real samples, the backbone model tends to detect the presence of forged regions. For instance, on real samples from FF++, the backbone focuses on specific facial areas such as the eyes and cheeks. In contrast, our method exhibits a more dispersed attention pattern throughout the image. This suggests that our detector does not rely on the presence or absence of artifacts to classify an image as real, but instead learns to assess whether the image conforms to the distribution of the real class. ii) For fake samples, both the backbone and RDBC focus on forged regions. However, our method covers broader regions. This can be attributed to the whitening module, which amplifies the Gaussianity gap between real and fake images. In this way, more artifacts will be exposed in the content-independent domain, and the generalization will be improved.

**Image Distributions.** Fig. 8 presents the t-SNE visualizations

of feature distributions from the source and target domains. Specifically, Fig. 8(a) and Fig. 8(b) show the distributions of real images. It can be observed that the backbone fails to align real images from the source and target domains. For instance, in Fig. 8(a), real samples from the source domain (blue circles) are densely clustered in the upper-left region, whereas those from the target domain (yellow and orange circles) are scattered across both the upper-right and lower-right regions. In contrast, features produced by our RDBC are uniformly distributed on the entire image, regardless of domain. This indicates that RDBC models real images in a domain-agnostic fashion, enabling an unbiased estimation of real features. Furthermore, Fig. 8(c) and Fig. 8(d) present comparisons between real and fake samples. In Fig. 8(c), fake samples (triangles) and real samples (circles) exhibit substantial overlap in their distributions. In contrast, RDBC demonstrates a clearer separation between real and fake samples. Together, the heatmap and t-SNE results provide complementary evidence for RDBC: the former shows reduced attention to artifact cues, while the latter reveals a more domain-invariant feature space. This suggests that the gain of our method comes not from stronger generator-specific traces, but from a more transferable criterion for modeling realism.

### E. Efficiency Analysis

Our RDBC imposes only light-weight computational overhead during training and inference. The additional operations (real distribution estimation and feature whitening) consist of simple statistical computations and linear transforms, thus no extra layers or large modules are added. As a result, per-batch training time remains virtually the same as that of the base detector. During the testing phase, the model merely applies a precomputed whitening transform (sampled from the learned real-image covariance) to features before the classifier. This single linear operation introduces negligible latency, so inference speed is essentially unchanged. Because the method is backbone-agnostic and only uses linear algebra routines, it can scale with both model capacity and dataset size.

## V. CONCLUSION

In this paper, we propose a novel direction for enhancing generalization by leveraging the distributional invariance of real data. Ideally, real images are captured through consistent physical imaging processes and can therefore be regarded as i.i.d. samples drawn from a common population distribution. So, their statistics can be inferred to follow a normal distribution, and the parameters of the normal distribution can be estimated using maximum likelihood estimation (MLE). This allows us to simulate the complete real-data distribution in the vicinity of the source-domain distribution as accurately as possible. Furthermore, to incorporate knowledge of the simulated population distribution into the training process, we exploit the inherent Gaussianity of real data as a discriminative cue and employ distribution-sampling-based whitening to amplify the Gaussianity gap between real and fake data. In summary, our method leverages the distributional characteristics of real data to identify non-real samples more effectively, thereby improving cross-domain generalization.

## REFERENCES

- [1] B. F. Labs, S. Batifol, A. Blattmann, F. Boesel, S. Consul, C. Diagne, T. Dockhorn, J. English, Z. English, P. Esser *et al.*, “Flux. 1 kontekst: Flow matching for in-context image generation and editing in latent space,” *arXiv preprint arXiv:2506.15742*, 2025.
- [2] T. Wang, X. Liao, K. P. Chow, X. Lin, and Y. Wang, “Deepfake detection: A comprehensive survey from the reliability perspective,” *ACM CSUR*, vol. 57, no. 3, pp. 1–35, 2024.
- [3] Z. Yan, Y. Zhao, S. Chen, M. Guo, X. Fu, T. Yao, S. Ding, Y. Wu, and L. Yuan, “Generalizing deepfake video detection with plug-and-play: Video-level blending and spatiotemporal adapter tuning,” in *CVPR*, 2025, pp. 12 615–12 625.
- [4] M.-H. Liu, X.-Q. Liu, X. Luo, and X.-S. Xu, “Data: Multi-disentanglement based contrastive learning for open-world semi-supervised deepfake attribution,” *IEEE TMM*, vol. 27, pp. 8239–8250, 2025.
- [5] M.-H. Liu, H. Cheng, T. Wang, X. Luo, and X.-S. Xu, “Learning real facial concepts for independent deepfake detection,” in *IJCAI*, 2025, pp. 1585–1593.
- [6] C. Kong, A. Luo, S. Wang, H. Li, A. Rocha, and A. C. Kot, “Pixel-inconsistency modeling for image manipulation localization,” *IEEE TPAMI*, vol. 47, pp. 4455–4472, 2025.
- [7] Y. Wang, Z. Huang, Z. Su, A. Prugel-Bennett, and X. Hong, “Penny-wise and pound-foolish in ai-generated image detection,” *IEEE TPAMI*, pp. 1–14, 2026.
- [8] R. Xia, D. Zhou, L. Yuan, J. Li, N. Wang, and X. Gao, “Ssd: Making face forgery clues evident again with self-steganographic detection,” *IEEE TPAMI*, pp. 1–17, 2026.
- [9] Y.-H. Han, T.-M. Huang, K.-L. Hua, and J.-C. Chen, “Towards more general video-based deepfake detection through facial component guided adaptation for foundation model,” in *CVPR*, 2025, pp. 22 995–23 005.
- [10] K. Sun, S. Chen, T. Yao, H. Liu, X. Sun, S. Ding, and R. Ji, “Diffusion-fake: Enhancing generalization in deepfake detection via guided stable diffusion,” in *NeurIPS*, 2024, pp. 101 474–101 497.
- [11] Z. Yan, Y. Luo, S. Lyu, Q. Liu, and B. Wu, “Transcending forgery specificity with latent space augmentation for generalizable deepfake detection,” in *CVPR*, 2024, pp. 8984–8994.
- [12] K. Shiohara and T. Yamasaki, “Detecting deepfakes with self-blended images,” in *CVPR*, 2022, pp. 18 699–18 708.
- [13] C. Wang and W. Deng, “Representative forgery mining for fake face detection,” in *CVPR*, 2021, pp. 14 923–14 932.
- [14] H. Cheng, Y. Guo, T. Wang, Q. Li, X. Chang, and L. Nie, “Voice-face homogeneity tells deepfake,” *ACM ToMM*, vol. 20, no. 3, pp. 1–22, 2023.
- [15] J. Cheng, Z. Yan, Y. Zhang, Y. Luo, Z. Wang, and C. Li, “Can we leave deepfake data behind in training deepfake detector?” in *NeurIPS*, 2024.
- [16] H. Cheng, Y. Guo, T. Wang, L. Nie, and M. Kankanhalli, “Diffusion facial forgery detection,” in *ACM MM*, 2024, p. 5939–5948.
- [17] P. Esser, S. Kulal, A. Blattmann, R. Entezari, J. Müller, H. Saini, Y. Levi, D. Lorenz, A. Sauer, F. Boesel, D. Podell, T. Dockhorn, Z. English, and R. Rombach, “Scaling rectified flow transformers for high-resolution image synthesis,” in *ICML*, 2024, pp. 1–13.
- [18] M. K. Johnson and H. Farid, “Exposing digital forgeries by detecting inconsistencies in lighting,” in *MM&Sec*, 2005, p. 1–10.
- [19] K. Kumari, S. Behrouzi, A. Pegoraro, and A.-R. Sadeghi, “Light2lie: Detecting deepfake images using physical reflectance laws,”
- [20] S. Hu, Y. Li, and S. Lyu, “Exposing gan-generated faces using inconsistent corneal specular highlights,” in *ICASSP*, 2021, pp. 2500–2504.
- [21] U. A. Ciftci, I. Demir, and L. Yin, “Fakecatcher: Detection of synthetic portrait videos using biological signals,” *TPAMI*, 2020.
- [22] E. P. Simoncelli and B. A. Olshausen, “Natural image statistics and neural representation,” *Annu. Rev. Neurosci.*, vol. 24, no. 1, pp. 1193–1216, 2001.
- [23] D. L. Ruderman, “The statistics of natural images,” *Netw. Comput. Neural Syst.*, vol. 5, no. 4, p. 517, 1994.
- [24] S. Nadarajah, “Gaussian dct coefficient models,” *Acta Appl. Math.*, vol. 106, no. 3, pp. 455–472, 2009.
- [25] D. P. Kingma and M. Welling, “Auto-encoding variational bayes,” in *ICLR*, 2014.
- [26] J. Thies, M. Zollhöfer, M. Stamminger, C. Theobalt, and M. Nießner, “Face2face: Real-time face capture and reenactment of RGB videos,” in *CVPR*, 2016, pp. 2387–2395.
- [27] S. Suwajanakorn, S. M. Seitz, and I. Kemelmacher-Shlizerman, “Synthesizing obama: learning lip sync from audio,” *ACM TOG*, vol. 36, no. 4, pp. 95:1–95:13, 2017.
- [28] T. Karras, S. Laine, and T. Aila, “A style-based generator architecture for generative adversarial networks,” in *CVPR*, 2019, pp. 4401–4410.
- [29] J. Bao, D. Chen, F. Wen, H. Li, and G. Hua, “Towards open-set identity preserving face synthesis,” in *CVPR*, 2018, pp. 6713–6722.
- [30] Y. Nirkin, Y. Keller, and T. Hassner, “Fsganv2: Improved subject agnostic face swapping and reenactment,” *IEEE TPAMI*, vol. 45, no. 1, pp. 560–575, 2023.
- [31] C. Xu, J. Zhang, M. Hua, Q. He, Z. Yi, and Y. Liu, “Region-aware face swapping,” in *CVPR*, 2022, pp. 7622–7631.
- [32] Z. Xu, H. Zhou, Z. Hong, Z. Liu, J. Liu, Z. Guo, J. Han, J. Liu, E. Ding, and J. Wang, “Styleswap: Style-based generator empowers robust face swapping,” in *ECCV*, 2022, pp. 661–677.
- [33] L. Li, J. Bao, H. Yang, D. Chen, and F. Wen, “Advancing high fidelity identity swapping for forgery detection,” in *CVPR*, 2020, pp. 5073–5082.
- [34] R. Chen, X. Chen, B. Ni, and Y. Ge, “Simsmap: An efficient framework for high fidelity face swapping,” in *ACM MM*, 2020, pp. 2003–2011.
- [35] X. Chen, B. Ni, Y. Liu, N. Liu, Z. Zeng, and H. Wang, “Simsmap++: Towards faster and high-quality identity swapping,” *IEEE TPAMI*, vol. 46, no. 1, pp. 576–592, 2023.
- [36] K. Kim, Y. Kim, S. Cho, J. Seo, J. Nam, K. Lee, S. Kim, and K. Lee, “Difface: Diffusion-based face swapping with facial guidance,” *PR*, vol. 163, p. 111451, 2025.
- [37] W. Zhao, Y. Rao, W. Shi, Z. Liu, J. Zhou, and J. Lu, “Diffswap: High-fidelity and controllable face swapping via 3d-aware masked diffusion,” in *CVPR*, 2023, pp. 8568–8577.
- [38] C. Hong, Y. Hsu, and T. Liu, “Contrastive learning for deepfake classification and localization via multi-label ranking,” in *CVPR*, 2024, pp. 17 627–17 637.
- [39] R. Xia, D. Zhou, D. Liu, J. Li, L. Yuan, N. Wang, and X. Gao, “Inspector for face forgery detection: Defending against adversarial attacks from coarse to fine,” *IEEE TIP*, vol. 33, pp. 4432–4443, 2024.
- [40] R. Xia, D. Zhou, D. Liu, L. Yuan, J. Li, N. Wang, and X. Gao, “Towards generalized proactive defense against face swapping with contour-hybrid watermark,” *arXiv preprint arXiv:2505.19081*, 2025.
- [41] S. Jia, C. Ma, T. Yao, B. Yin, S. Ding, and X. Yang, “Exploring frequency adversarial attacks for face forgery detection,” in *CVPR*, 2022, pp. 4093–4102.
- [42] I. Masi, A. Killekar, R. M. Mascarenhas, S. P. Gurudatt, and W. AbdAlmageed, “Two-branch recurrent network for isolating deepfakes in videos,” in *ECCV*, 2020, pp. 667–684.
- [43] X. Wu, Z. Xie, Y. Gao, and Y. Xiao, “Sstnet: Detecting manipulated faces through spatial, steganalysis and temporal features,” in *ICASSP*, 2020, pp. 2952–2956.
- [44] C. Tan, H. Liu, Y. Zhao, S. Wei, G. Gu, P. Liu, and Y. Wei, “Rethinking the up-sampling operations in cnn-based generative network for generalizable deepfake detection,” in *CVPR*, 2024, pp. 28 130–28 139.
- [45] J. Cheng, Z. Yan, Y. Zhang, L. Hao, J. Ai, Q. Zou, C. Li, and Z. Wang, “Stacking brick by brick: Aligned feature isolation for incremental face forgery detection,” in *CVPR*, 2025, pp. 13 927–13 936.
- [46] S. Li, J. Leng, C. Kuang, M. Tan, and X. Gao, “Video-level language-driven video-based visible-infrared person re-identification,” *IEEE TIFS*, vol. 20, pp. 5505–5520, 2025.
- [47] Y. Luo, Y. Zhang, J. Yan, and W. Liu, “Generalizing face forgery detection with high-frequency features,” in *CVPR*, 2021, pp. 16 317–16 326.
- [48] K. Sun, S. Chen, T. Yao, Z. Zhou, J. Ji, X. Sun, C.-W. Lin, and R. Ji, “Towards general visual-linguistic face forgery detection,” in *CVPR*, 2025, pp. 19 576–19 586.
- [49] T. Oorloff, S. Koppiseti, N. Bonettini, D. Solanki, B. Colman, Y. Yaacob, A. Shahriyari, and G. Bharaj, “Avff: Audio-visual feature fusion for video deepfake detection,” in *CVPR*, 2024, pp. 27 102–27 112.
- [50] G. Tkačik, J. S. Prentice, J. D. Victor, and V. Balasubramanian, “Local statistics in natural scenes predict the saliency of synthetic textures,” *PNAS*, vol. 107, no. 42, pp. 18 149–18 154, 2010.
- [51] Y. Zhang, J. Nie, X. Tian, M. Gong, K. Zhang, and B. Han, “Detecting generated images by fitting natural image distributions,” in *NeurIPS*, 2025.
- [52] D. Zoran and Y. Weiss, “Natural images, gaussian mixtures and dead leaves,” in *NeurIPS*, 2012, pp. 1–9.
- [53] N. Zhong, M. Zou, Y. Xu, Z. Qian, X. Zhang, B. Wu, and K. Ma, “Self-supervised ai-generated image detection: A camera metadata perspective,” *IEEE TPAMI*, 2026.
- [54] J. Ballé, V. Laparra, and E. P. Simoncelli, “End-to-end optimized image compression,” in *ICLR*, 2017.
- [55] M. J. Wainwright and E. Simoncelli, “Scale mixtures of gaussians and the statistics of natural images,” in *NeurIPS*, 1999, pp. 1–7.
- [56] B. A. Olshausen and D. J. Field, “Natural image statistics and efficient coding,” *Netw. Comput. Neural Syst.*, vol. 7, no. 2, p. 333, 1996.

- [57] M. Lebrun, M. Colom, A. Buades, and J.-M. Morel, “Secrets of image denoising cuisine,” *Acta Numer.*, vol. 21, pp. 475–576, 2012.
- [58] J. Schmee, “An introduction to multivariate statistical analysis,” 1986.
- [59] Y. J. Wong and T. K. Ng, “Local statistics for generative image detection,” in *ICASSP*, 2025, pp. 1–5.
- [60] J. Frank, T. Eisenhofer, L. Schönherr, A. Fischer, D. Kolossa, and T. Holz, “Leveraging frequency analysis for deep fake image recognition,” in *ICML*, 2020, pp. 3247–3258.
- [61] M. Tan and Q. V. Le, “Efficientnet: Rethinking model scaling for convolutional neural networks,” in *ICML*, vol. 97, 2019, pp. 6105–6114.
- [62] L. Li, J. Bao, T. Zhang, H. Yang, D. Chen, F. Wen, and B. Guo, “Face x-ray for more general face forgery detection,” in *CVPR*, 2020, pp. 5000–5009.
- [63] Y. Ni, D. Meng, C. Yu, C. Quan, D. Ren, and Y. Zhao, “CORE: consistent representation learning for face forgery detection,” in *CVPRW*, 2022, pp. 12–21.
- [64] J. Cao, C. Ma, T. Yao, S. Chen, S. Ding, and X. Yang, “End-to-end reconstruction-classification learning for face forgery detection,” in *CVPR*, 2022, pp. 4103–4112.
- [65] S. Dong, J. Wang, R. Ji, J. Liang, H. Fan, and Z. Ge, “Implicit identity leakage: The stumbling block to improving deepfake detection generalization,” in *CVPR*, 2023, pp. 3994–4004.
- [66] Z. Yan, Y. Zhang, Y. Fan, and B. Wu, “UCF: uncovering common features for generalizable deepfake detection,” in *ICCV*, 2023, pp. 22 355–22 366.
- [67] J. Tian, P. Chen, C. Yu, X. Fu, X. Wang, J. Dai, and J. Han, “Learning to discover forgery cues for face forgery detection,” *IEEE TIFS*, vol. 19, pp. 3814–3828, 2024.
- [68] T. Qiao, S. Xie, Y. Chen, F. Retraint, and X. Luo, “Fully unsupervised deepfake video detection via enhanced contrastive learning,” *IEEE TPAMI*, vol. 46, no. 7, pp. 4654–4668, 2024.
- [69] J. Choi, T. Kim, Y. Jeong, S. Baek, and J. Choi, “Exploiting style latent flows for generalizing deepfake video detection,” in *CVPR*, 2024, pp. 1133–1143.
- [70] J. Zhou, Y. Li, B. Wu, B. Li, J. Dong *et al.*, “Freqblender: Enhancing deepfake detection by blending frequency knowledge,” in *NeurIPS*, 2024, pp. 44 965–44 988.
- [71] Z. Yan, J. Wang, P. Jin, K.-Y. Zhang, C. Liu, S. Chen, T. Yao, S. Ding, B. Wu, and L. Yuan, “Orthogonal subspace decomposition for generalizable ai-generated image detection,” in *ICML*, 2025, pp. 1–13.
- [72] L. Ma, Z. Yan, J. Xu, Y. Chen, Q. Guo, Z. Bi, Y. Liao, and H. Lin, “From specificity to generality: Revisiting generalizable artifacts in detecting face deepfakes,” in *NeurIPS*, 2025.
- [73] W. Guan, W. Wang, J. Dong, and B. Peng, “Improving generalization of deepfake detectors by imposing gradient regularization,” *IEEE TIFS*, vol. 19, pp. 5345–5356, 2024.
- [74] A. Rössler, D. Cozzolino, L. Verdoliva, C. Riess, J. Thies, and M. Nießner, “Faceforensics++: Learning to detect manipulated facial images,” in *ICCV*, 2019, pp. 1–11.
- [75] Y. Li, X. Yang, P. Sun, H. Qi, and S. Lyu, “Celeb-df: A large-scale challenging dataset for deepfake forensics,” in *CVPR*, 2020, pp. 3204–3213.
- [76] B. Dolhansky, J. Bitton, B. Pflaum, J. Lu, R. Howes, M. Wang, and C. C. Ferrer, “The deepfake detection challenge (dfdc) dataset,” *arXiv preprint arXiv:2006.07397*, 2020.
- [77] X. Yang, Y. Li, and S. Lyu, “Exposing deep fakes using inconsistent head poses,” in *ICASSP*, 2019, pp. 8261–8265.
- [78] A. Dosovitskiy, L. Beyer, A. Kolesnikov, D. Weissenborn, X. Zhai, T. Unterthiner, M. Dehghani, M. Minderer, G. Heigold, S. Gelly, J. Uszkoreit, and N. Houlsby, “An image is worth 16x16 words: Transformers for image recognition at scale,” in *ICLR*, 2021.